

JGR Space Physics

RESEARCH ARTICLE

10.1029/2021JA029609

Key Points:

- A very narrow band whistler wave and electron cyclotron harmonic waves are simultaneously observed in the magnetosphere separatrix region
- The electron loss-cone distributions are continuously detected while the two kinds of waves are observed
- The two kinds of waves are probably excited by the electron loss-cone instability

Correspondence to:

Q. Lu and R. Wang,
qmlu@ustc.edu.cn;
rswan@ustc.edu.cn

Citation:

Yu, X., Lu, Q., Wang, R., Gao, X., Sang, L., & Wang, S. (2021). Simultaneous observation of whistler waves and electron cyclotron harmonic waves in the separatrix region of magnetopause reconnection. *Journal of Geophysical Research: Space Physics*, 126, e2021JA029609. <https://doi.org/10.1029/2021JA029609>

Received 27 MAY 2021
 Accepted 9 SEP 2021

Simultaneous Observation of Whistler Waves and Electron Cyclotron Harmonic Waves in the Separatrix Region of Magnetopause Reconnection

Xiancai Yu^{1,2,3} , Quanming Lu^{1,2,3} , Rongsheng Wang^{1,2,3} , Xinliang Gao^{1,2,3} , Longlong Sang^{1,2,3}, and Shui Wang^{1,2}

¹CAS Key Laboratory of Geospace Environment, Department of Geophysics and planetary Science, University of Science and Technology of China, Hefei, China, ²CAS Center for Excellence in Comparative Planetology, Hefei, China, ³Mengcheng National Geophysical Observatory, School of Earth and Space Sciences, University of Science and Technology of China, Hefei, China

Abstract A variety of plasma waves have been observed in the separatrix region during magnetic reconnection, and their roles on reconnection and exciting mechanisms are still controversial. In this paper, we report the whistler wave with a very narrow frequency band just above half of the electron cyclotron frequency in the separatrix region. This whistler wave is accompanied with the electron cyclotron harmonic (ECH) waves. The ECH waves have frequencies between the first and fifth harmonic of electron cyclotron frequency f_{ce} . The wave normal angle of the whistler waves is $\sim 20^\circ \sim 40^\circ$, meaning the quasi-parallel propagation, while the ECH waves propagate perpendicular to the background magnetic field with $\theta \sim 87^\circ \pm 2^\circ$. In the separatrix region, the electrons have a loss-cone distribution while these two kinds of waves are observed. Based on the linear theory, such an electron distribution is unstable for both whistler waves and ECH waves. It indicates that these two kinds of waves are generated by the electron loss-cone instability.

1. Introduction

In the magnetosphere, whistler waves and electron cyclotron harmonic (ECH) waves are commonly observed (Breuillard et al., 2016; Gao et al., 2016; Huang et al., 2016, 2017; Lou et al., 2018; Wilder et al., 2016; Zhou et al., 2009, 2016). Whistler waves are electromagnetic waves which generally have a frequency below the electron cyclotron frequency f_{ce} , and their property is shown as the right-handed circular polarization (Deng & Matsumoto, 2001; Graham et al., 2016; Gurnett et al., 1976; Stenzel, 1999). While ECH waves are electrostatic emissions that nearly propagate perpendicular to the magnetic field (Gurnett & Bhattacharjee, 2005; Lou et al., 2018), and their harmonic bands are frequently observed between the integral multiples of the electron cyclotron frequency $(n + 1)f_{ce}$, concentrated in the narrow bands near $(n + 1/2)f_{ce}$ (Gurnett et al., 1979; Kennel et al., 1970). A series of observations showed that whistler waves and ECH waves are committed to electron scattering and precipitation (Horne et al., 2003; Kurita et al., 2014; Lou et al., 2021; Thorne et al., 2010).

Generally, whistler waves can be excited by the electron temperature anisotropies whose perpendicular temperature is larger than parallel temperature (Graham et al., 2016; Kennel & Petschek, 1966), and electron beams (Bell & Buneman, 1964; Huang et al., 2016, 2017, 2020). In addition, Goldman et al. (2014) reported that the Čerenkov emission from electrostatic solitary waves can also excite the whistler waves. In contrast, it is believed that ECH waves can be driven by the electrostatic instability whose electron phase space density $f(v)$ has a positive gradient in the perpendicular direction $\partial f / \partial v_\perp > 0$ (Ashour-Abdalla & Kennel, 1978), such as the ring, loss cone, or shell electron velocity distribution (Li et al., 2020; Liu et al., 2018; Umeda et al., 2007; Wu et al., 2020).

Previous observations have shown that whistler waves and ECH waves are often observed in the magnetic reconnection of the magnetosphere (Deng & Matsumoto, 2001; Huang et al., 2016, 2017; Jiang et al., 2019; Wang et al., 2019; Wilder et al., 2016; Zhao et al., 2021; Zhong et al., 2021), especially in the separatrix region and electron diffusion region (EDR) (Cao et al., 2017; Huang et al., 2016; Li et al., 2020; Tang et al., 2013; Viberg et al., 2013; Zhou et al., 2011, 2016). Huang et al. (2016) reported two types of whistler waves in the

pileup region and separatrix region of magnetotail reconnection. They suggested that the waves in the pileup region may be generated by the electron temperature anisotropy, while the waves in the separatrix region were probably generated by the electron beam or Čerenkov emission from electrostatic solitary waves. In Huang et al. (2017), they presented the full image of whistler waves in the magnetotail reconnection region based on Cluster data, and found that the occurrence rate of the whistler waves is larger in the separatrix region and in the pileup region, but is very small in the vicinity of the x-line. Le Contel et al. (2016) showed whistler waves at $f \sim 0.5f_{ce}$ in the magnetopause reconnection, and these waves are propagated quasi-parallel or obliquely to the magnetic field toward the reconnection region. Graham et al. (2016) found that the large-amplitude whistler waves in the separatrix regions of magnetopause reconnection can be driven by the electron loss cone distributions. For the ECH waves, Zhou et al. (2016) found that ECH waves can exist at the magnetosheath separatrix region of magnetopause reconnection and the energy dissipation contributed by the ECH waves was negligible in the diffusion regions. Li et al. (2020) reported that the large-amplitude ECH waves around the EDR of magnetopause reconnection were driven by electron crescent distributions, and they suggested that the large amplitude ECH waves can effectively thermalize and scatter electrons. However, as we know, there is no report showing the simultaneous existence of whistler waves and ECH waves in the reconnection region. In this paper, we present the simultaneous observations of the whistler waves and the ECH waves in the magnetosphere separatrix region at the dayside magnetopause, and the electrons in this region display the loss-cone distribution. Based on the electron distributions and the linear theory, we infer that the whistler waves and the ECH waves are excited by the electron loss-cone instability. Our results provide more insights on the excitation of plasma waves in magnetic reconnection.

2. Database and MMS Observations

In this paper, we mainly use the electric field, magnetic field, and plasma data of MMS at the burst mode (Ergun et al., 2016; Le Contel et al., 2014; Lindqvist et al., 2014; Pollock et al., 2016; Russell et al., 2016). On November 12, 2015, MMS was located at around $(11.3, 2.0, -0.7)R_E$ (R_E is the Earth's radius) in the Geocentric Solar Ecliptic (GSE) coordinate system and crossed the magnetopause current sheet at $\sim 05:57$ UT. The largest separation between the four MMS satellites was ~ 20 km at that time. Based on the minimum variance analysis of the MMS2 magnetic field (MVA; Sonnerup & Scheible, 1998), we obtain the local boundary normal coordinates with $L = (0.2844, -0.0174, 0.9585)$, $M = (-0.0628, 0.9974, 0.0367)$, and $N = (-0.9566, -0.0706, 0.2826)$ relative to the GSE coordinates.

An overview of the magnetopause crossing in the local boundary normal coordinates is shown Figure 1. At around 05:57:02 UT, the magnetic field B_L component reverses from ~ 47 nT to ~ -30 nT (Figure 1a) with an increased plasma density (Figure 1g) and a reduced electron temperature (Figure 1h) are detected, which indicates that the satellite crosses the magnetopause current sheet from the magnetosphere side to the magnetosheath side. As the spacecraft traverses the current sheet, the ion bulk flow V_{iL} changes from a positive value to a negative value (Figure 1e). In the northward ion flow region ($V_{iL} > 0$), the magnetic field component B_M varies from a positive value to a negative value, then back to a positive value again with the changes of B_L (Figure 1a), which is consistent with the hexapolar Hall magnetic field of asymmetric reconnection in the PIC simulations of Sang et al. (2019). In this event, the ratio between the magnetosphere magnetic field and magnetosheath magnetic field is about 2, and their density ratio is about 1/14, which conforms to the generation condition of the hexapolar Hall magnetic field in the PIC simulations of Sang et al. (2019). When the spacecraft enters the southward ion flow region ($V_{iL} < 0$), the magnetic field component B_M remains positive (Figure 1a). Based on the observed characteristics of the Hall magnetic field and the ion bulk flows, we conclude that the spacecraft crosses the ion diffusion region of magnetopause reconnection from the northward of the X-line to the southward, as shown in Figure 1k. Throughout the crossing, the electron bulk flow also reverses from a positive value to a negative value (Figure 1d), and a strong southward electron flow ($V_{eL} < 0$) is observed in the magnetosphere side of the current sheet and the northward of X-line around 05:56:55 UT. Based on the Hall current system, in this side, the northward electron flows are the reconnection electron northward outflows, while the southward electron flows correspond to the inflowing electrons in the separatrix region. Therefore, the satellite crosses the magnetosphere separatrix region. In the magnetosphere separatrix region, the strong out-of-plane electron flow V_{eM} (negative) and ion flow V_{iM} (positive) are observed (Figures 1d and 1f), and the speed of ion flow V_{iM} is up to ~ 150 km/s $\sim 0.5V_A$ (where

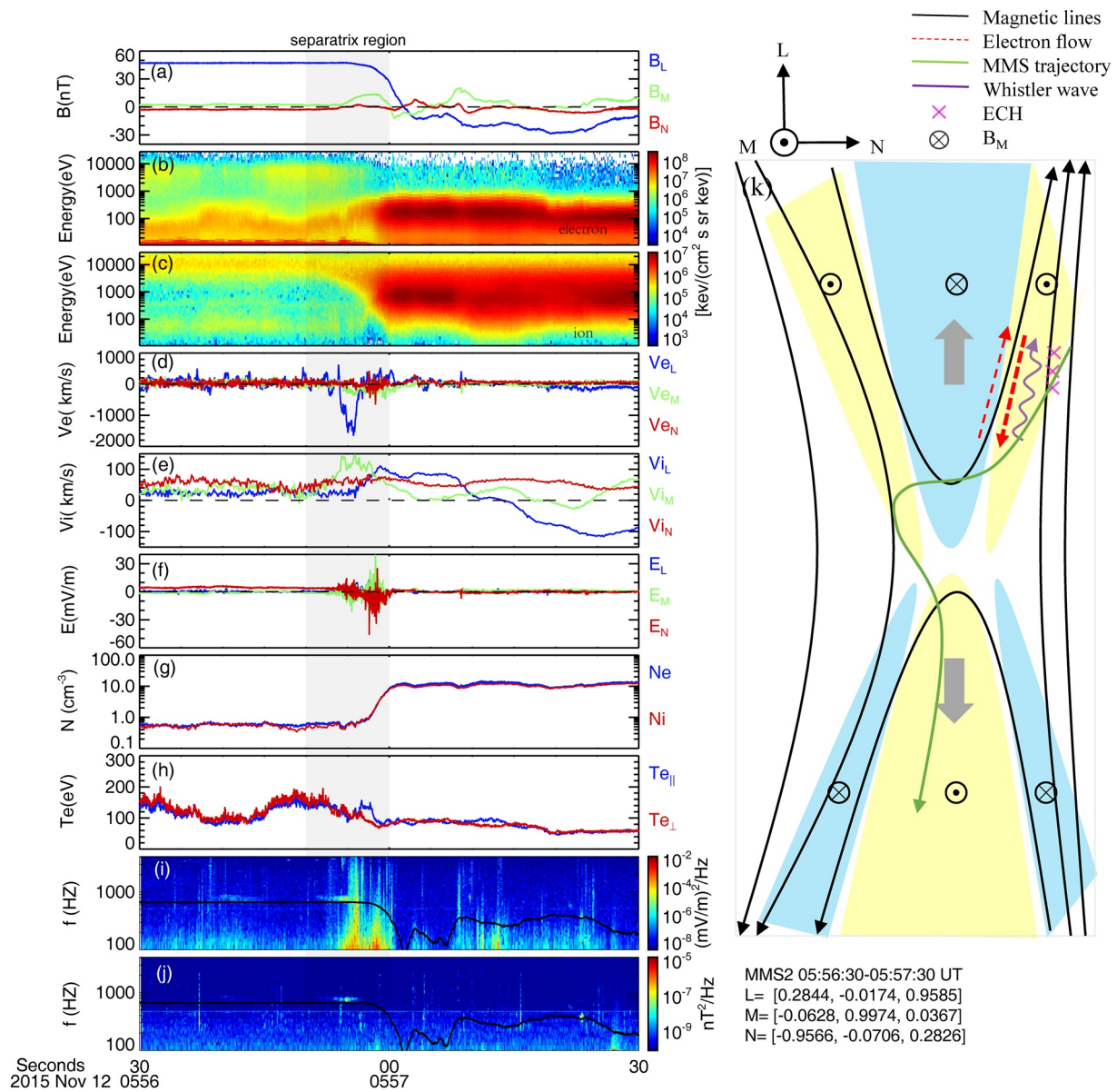


Figure 1. Overview of the magnetopause current sheet crossing. (a) Magnetic field B . (b–c) Electron and ion energy spectrum. (d–e) Velocities of electrons and ions in three directions. (f) Electric field E . (g) Electron and ion number densities. (h) Electron temperature. (i–j) The power spectrum of E and B , and the black curves are $0.5f_{ce}$. (k) A schematic illustration of the magnetopause crossing, in which the MMS trajectory is represented by the green curve, and the region in pale blue (yellow) indicates the negative (positive) B_M . The vertical gray bar represents the crossing separatrix region.

V_A is the ion Alfvén speed given by $V_A^2 = B_{sp} B_{sh} (B_{sp} + B_{sh}) / (\mu_0 m_i n_{isp} B_{sh} + \mu_0 m_i n_{ish} B_{sp})$ with subscripts “sp” and “sh” denoting the magnetosphere and magnetosheath, and there are no obvious out-of-plane flows near the X-line in the magnetosheath side, which is well consistent with the simulations of the asymmetric magnetic reconnection (Burch et al., 2016; Lapenta et al., 2017; Phan et al., 2016; Sang et al., 2019; Wang et al., 2017; Yu et al., 2019). In addition, the speed of inflowing electron approaches 2,000 km/s in the separatrix region, much larger than the outflow speed (≤ 400 km/s, Figure 1d), and such strong speed of the inflowing electron has also been observed in the Yu et al. (2019).

In the magnetosphere separatrix region, the electric field has large fluctuations (Figure 1f), and we observe the existence of electrostatic and electromagnetic plasma waves from the electric and magnetic power spectrum (Figures 1i and 1j) during the time period 05:56:50–05:57:00 UT. The detailed analyses of the plasma

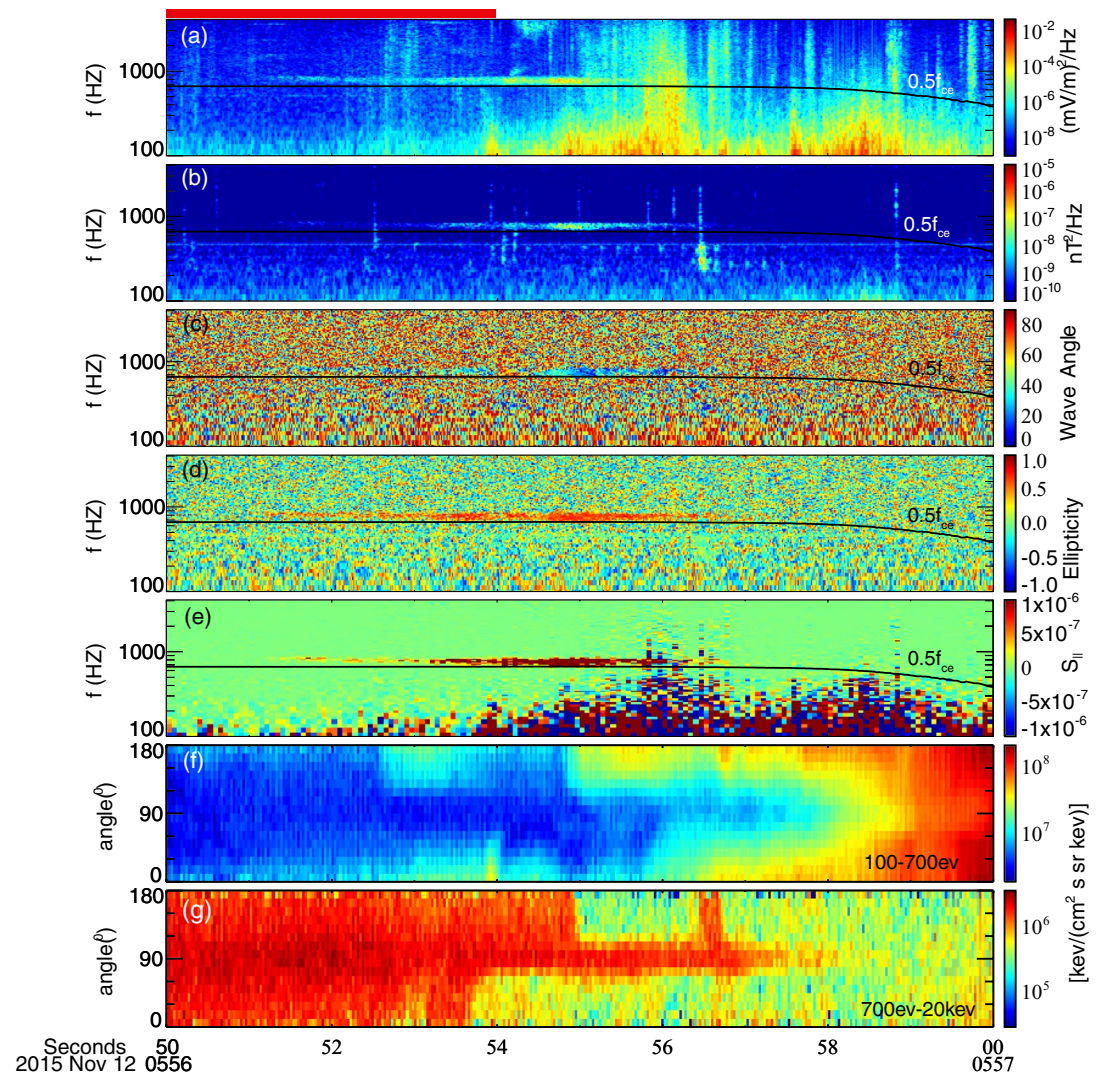


Figure 2. The observations of waves in the separatrix region. (a and b) The power spectrum of E and B. (c) Wave normal angle. (d) The ellipticity. (e) The Poynting vector in parallel direction S_{\parallel} . (f–g) The pitch angle distribution of the electrons at energies 100–700 eV and 700 eV–20 keV. The black curves shown in (a–e) are $0.5f_{ce}$.

waves in this region are displayed in the Figure 2. From the omnidirectional electric and magnetic power spectrum (Figures 2a and 2b), a high-frequency electromagnetic emission is detected during the time period 05:56:51–05:56:56 UT, and its frequency is around 750 Hz $\sim 0.6f_{ce}$. Strong broadband electrostatic emissions are detected after 05:56:56 UT, and their parallel electric field has solitary bipolar structures (not shown). Thus, we think that the broadband emission is associated with the electrostatic solitary wave (Cattell et al., 2005; Matsumoto et al., 2003; Wang et al., 2014; Yu et al., 2021). Figures 2c–2d show the wave angle, and the ellipticity of the high-frequency electromagnetic emission obtained from the spectral matrix. The wave normal angle of the high-frequency electromagnetic emission varies from 20° to 40°, which means that its propagation is quasi-parallel or oblique. Furthermore, the ellipticity of the high-frequency electromagnetic emission is close to +1, indicating that it is a right-hand circular polarization. Based on these analyses, the high-frequency electromagnetic emission can be recognized as whistler waves with a narrow frequency band around $f \sim 0.6f_{ce} \sim 750$ Hz.

In addition, the Poynting vector of the waves in the parallel direction is positive ($S_{\parallel} > 0$, shown in the Figure 2e). Therefore, the whistler waves in the magnetosphere separatrix region are propagating away from the reconnection x-line along the direction parallel to the magnetic field. Based on the observations, we

can use the averaging $|E/B|$ to estimate the phase speed of the whistler waves v_{ph} , which is about 25,000–30,000 km/s. The wave wavelength in the parallel direction is about $\lambda_{\parallel} = v_{ph}/f \sim 31 - 37$ km based on $f \sim 750$ Hz. Thus, the speed of the resonant electrons calculated by the gyroresonance condition is about $v_{lres} = (f - f_{ce})\lambda_{\parallel} \sim 15600 - 18700$ km/s (Kennel & Petschek, 1966; Vaivads et al., 2007).

It is worth noting that a high-frequency electrostatic wave is simultaneously observed in the separatrix region when the whistler waves are detected (marked by red color bar on the top of Figure 2), and the details are showed in Figure 3. The high-frequency electrostatic waves are mainly observed during two sub-periods 05:56:51.00–05:56:51.55 UT and 05:56:53.20–05:56:53.75 UT, marked with A and B, respectively. Figures 3a–3d show the power spectrum of E_{\parallel} and E_{\perp} from a low frequency (100 Hz) to near the electron plasma frequency (red curves). Unfortunately, the electric field power spectrum calculated by the electric field data in short bursts of 65,536 sample/s (hmfe) is only available in the period of B ($f > 4096$ Hz, as shown in Figures 3a and 3c). From the power spectrum of the E_{\perp} (Figures 3c and 3d), we can see that the high-frequency electrostatic waves exist as a series of harmonic bands separated by $(n + 1)f_{ce}$, and other properties of the high-frequency electrostatic waves at two sub-periods A and B are presented in Figures 3e–3i and Figures 3j–3n, respectively. In the sub-period 05:56:53.20–05:56:53.75 UT (B), the peaks of wave power are observed in a range between $\sim 1,500$ Hz and 8,000 Hz, i.e., between the first and fifth harmonic of f_{ce} (Figure 3j). The waveforms of the high-frequency E_{\parallel} and E_{\perp} are shown in Figure 3k, and the perpendicular electric field E_{\perp} is much larger than the parallel electric field E_{\parallel} . Figures 3m–3n present the diagrams of electric fields obtained by the MVA of high-frequency electric fields, in which max, int, and min represent the maximum, intermediate, and minimum variance direction of the electron field. From the electric field diagrams, we can see that the maximum variance direction of high-frequency electrostatic waves are approximately $87^{\circ} \pm 2^{\circ}$ with respect to the background magnetic field B, and the wave fluctuations exhibit an approximately linear polarization. All properties of the high-frequency electrostatic waves observed in the period of B are in accordance with the characteristics of the ECH waves. In the sub-period 05:56:51.00–05:56:51.55 UT (A), the wave power is only observed in a range between the first and third harmonic of f_{ce} due to the lack of electric field data in short bursts of 65,536 samples/s, and other properties of these waves are similar to those observed in the sub-period B. Thus, the high-frequency electrostatic waves observed in the sub-periods A and B are the ECH waves.

In this separatrix region, the pitch angle distributions of the electrons are displayed in Figures 2f and 2g, in which the energy fluxes of low energy electron (100–700 eV) are shown as the field-aligned distribution ($\sim 0^{\circ}$ and/or $\sim 180^{\circ}$), but the energy fluxes of high energy electrons (700 eV–20 keV) are significantly enhanced around the perpendicular direction ($\sim 90^{\circ}$). In order to analyze the generation of the whistler waves and the ECH waves, we study the detailed electron distribution where the power of these two waves is the highest. Figures 4a and 4b show the electron phase-space density $f(v_e)$ as a function of electron velocity v_e for whistler waves and ECH waves in three directions, in which the black, red, and blue colors represent the perpendicular, antiparallel, and parallel directions, respectively. In this paper, we fit the electron distributions by summing up multiple components with the subtracted bi-Maxwellian distribution functions with drift velocity when the whistler waves and ECH waves are observed:

$$f(v_{\parallel}, v_{\perp}) = \frac{N}{\pi^{3/2} v_{th\perp}^2 v_{th\parallel}} \exp\left(-\frac{v_{\parallel}^2 - v_d^2}{v_{th\parallel}^2}\right) \left[\Delta \exp\left(-\frac{v_{\perp}^2}{v_{th\perp}^2}\right) + \frac{(1 - \Delta)}{(1 - \beta)} \left(\exp\left(-\frac{v_{\perp}^2}{v_{th\perp}^2}\right) - \exp\left(-\frac{v_{\perp}^2}{\beta v_{th\perp}^2}\right) \right) \right] \quad (1)$$

where $v_{th\parallel} = \sqrt{2kT_{\parallel}/m_e}$ and $v_{th\perp} = \sqrt{2kT_{\perp}/m_e}$ represent the parallel and perpendicular thermal velocities based on the parallel T_{\parallel} and perpendicular temperature T_{\perp} of electrons, respectively. N denotes the number density and v_d is the electron drift velocity. The parameters Δ and β are the loss cone depth and width, which can control the shape of the loss cone distribution. If $\Delta = 1$ or $\beta = 0$, Equation 1 is reduced to the drift bi-Maxwellian distribution. Table 1, and Table 2 list the fitting parameters of the whistler waves and the ECH waves, respectively.

For the whistler waves, the electron phase-space density $f(v_e)$ at $\theta = 180^{\circ}$ is larger than $\theta = 0^{\circ}$ and $\theta = 90^{\circ}$ for the electron velocity $v_e \leq 15000$ km/s, and then $f(v_e)$ is significantly larger at $\theta = 90^{\circ}$ for the $v_e \geq 15000$ km/s, forming a loss cone distribution at the magnetosphere side (Figure 4a). Figure 4c shows the 2-D electron velocity distribution when the whistler waves are observed, and it is consistent with the loss cone distribution. To investigate the instabilities, we use the dispersion equation solver BO (Xie, 2019) to solve

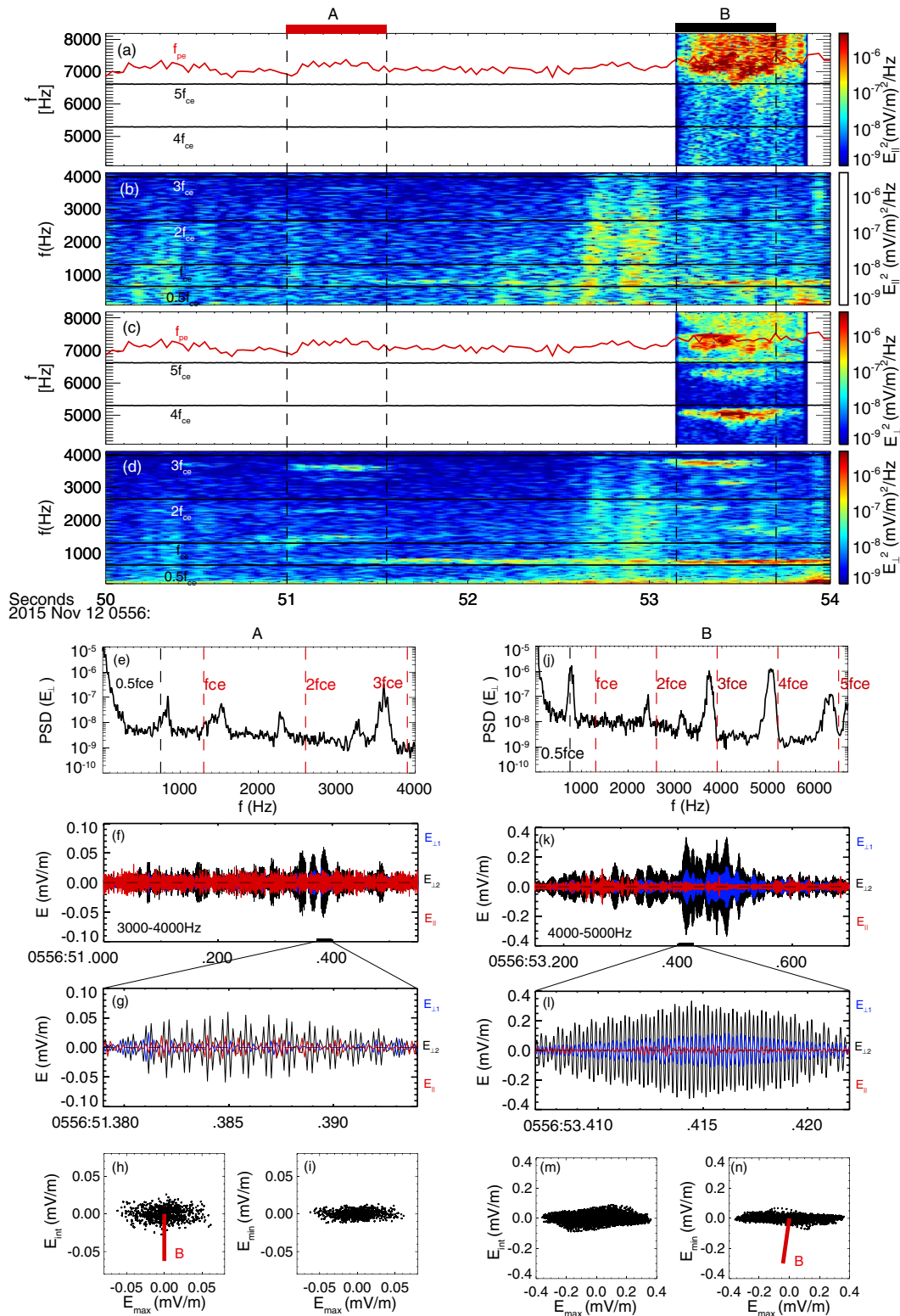


Figure 3. The observations of electron cyclotron harmonic waves in the separatrix region during two sub-periods A (05:56:51.00–05:56:51.55 UT) and B (05:56:53.20–05:56:53.75 UT). (a and b) The power spectrum of the E_{\parallel} and E_{\perp} . (e–i) and (j–n) show the wave properties during sub-periods A and B, respectively. (e) and (j) are the power spectral density of E_{\perp} . (f) and (k) are the electric fields in field-aligned coordinates (FAC). (g) and (l) are the zoom-in view of the electric field in FAC. (h) and (m) are the hodogram of E_{\max} versus E_{\min} . (i) and (n) are the hodograms of E_{\max} versus E_{\parallel} . The red lines in (h) and (n) denote the direction of the background magnetic field.

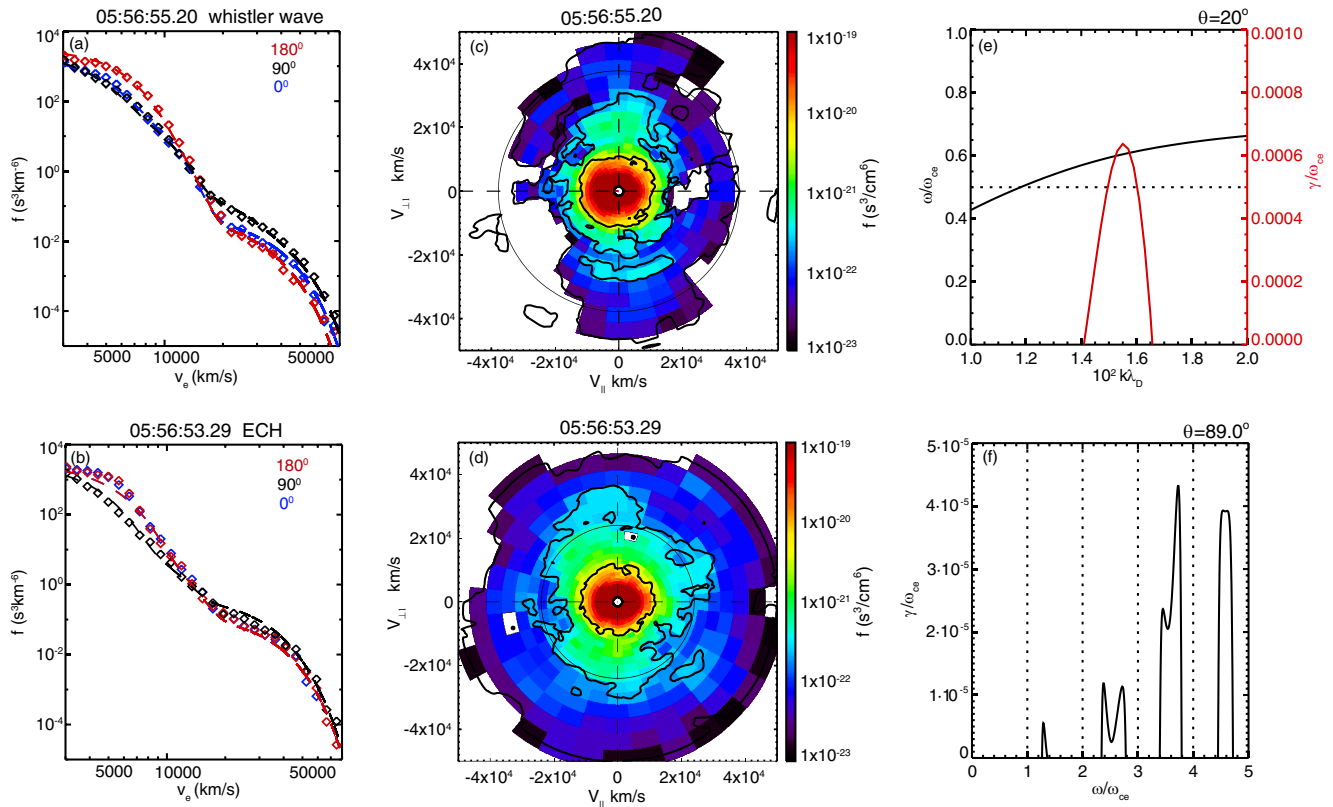


Figure 4. The electron distributions and dispersion relations. (a and b) Diagrams of the electron phase-space density $f(v_e)$ versus electron velocity v_e for whistler waves ($\sim 05:56:55.2$ UT) and ECH waves ($\sim 05:56:53.29$ UT) in three directions, in which the black, red, and blue colors are the perpendicular, antiparallel, and parallel directions, respectively. The rhombuses represent the observed value, and the lines are the fitting result. (c and d) The 2-D electron velocity distribution functions for the whistler waves and electron cyclotron harmonic (ECH) waves, in which V_{\parallel} is along B and V_{\perp} is along $E \times B$. (e) Dispersion relation of the unstable whistler waves and the growth rate, represented by black and red lines, respectively. (f) Dispersion relation of the unstable ECH waves.

the dispersion relation of whistler waves at $\theta = 20^\circ$, and we use the fitting parameters in Table 1 and the local magnetic field $|B|$ as the input parameters. Figure 4e shows the dispersion relation and the growth rate of the whistler waves, from which we can see that the frequency of the wave mode at the maximum growth rate is $\sim 0.6\omega_{ce}$, and the corresponding phase speed is $v_{ph} = \omega/k \sim 19000$ km/s, which is similar to the observations.

For the ECH waves, the electron phase-space densities shown in Figures 4b and 4d also display the loss-cone distribution, in which field-aligned distribution of the electrons is dominant at the low energy bands,

Table 1

The Electron Components Used to Fit the Measured Electron Distribution During 05:56:55.1–05:56:55.3 UT by Summation of Subtracted Bi-Maxwellian Distribution With Drift Velocity

Component	N (m^{-3})	v_d (km/s)	T_{\parallel} (eV)	T_{\perp} (eV)	Δ	β
1	6.5E5	−1.0E6	45	30	1.0	0.0
2	1.5E5	0.0	110	110	1.0	0.0
3	1.0E4	−6.0E6	80	800	1.0	0.0
4	2.0E4	0.0	1,000	1,800	1.0	0.0
5	4.0E3	3.0E6	2,000	2,500	1.0	0.0

Note. N is the number density. T_{\parallel} and T_{\perp} are the electron parallel and perpendicular temperatures. The parameters Δ and β are the loss cone depth and width, respectively.

Table 2

The Electron Components Used to Fit the Measured Electron Distribution During 05:56:53.2–05:56:53.4 UT by Summation of Subtracted Bi-Maxwellian Distribution With Drift Velocity

Component	N (m^{-3})	v_d (km/s)	T_{\parallel} (eV)	T_{\perp} (eV)	Δ	β
1	7.0E5	0.0	45	30	1.0	0.0
2	5.0E4	0.0	150	135	1.0	0.0
3	1.5E4	0.0	1,200	1,300	0.2	0.1
4	1.5E4	0.0	2,000	2,000	0.8	0.5

Note. N is the number density. T_{\parallel} and T_{\perp} are the electron parallel and perpendicular temperatures. The parameters Δ and β are the loss cone depth and width, respectively.

but the electrons become anisotropic at the high energy bands (especially at $E \sim 700$ eV corresponding speed $v_e \sim 15,000$ km/s). Similarly, we use the dispersion equation solver BO to solve the dispersion relation of ECH waves, and we use the fitting parameters in Table 2 as the input parameters. Based on the observations, we set the wave normal angle to $\theta = 89^\circ$. From solvation of the dispersion relation for the model distribution (Figure 4f), we find several unstable ECH modes, and the maximum growth rate is about $4.3 \times 10^{-5} \omega_{ce}$ between the third and fourth harmonics, consistent with the observation in Figure 3j. Therefore, we conjecture that the whistler waves and the ECH waves may be generated by the electron loss-cone distributions in the separatrix region.

3. Discussion and Summary

In this paper, we first present the simultaneous observation of the whistler waves and the ECH waves in the magnetosphere separatrix region. The whistler waves with a narrow band of about $0.6 f_{ce}$ propagate quasi-parallel to the background magnetic field, and their wave normal angle is about $20^\circ - 40^\circ$. The Poynting vector of these waves in the parallel direction is positive, indicating that the whistler waves propagate away from the reconnection x-line in the direction parallel to the magnetic field. For the ECH waves, the wave power is observed in a range between the first and fifth harmonic of the electron cyclotron frequency f_{ce} , and the wavevector k is nearly perpendicular to the background magnetic field by minimum variance analysis, which is $\theta = 87^\circ \pm 2^\circ$. In addition, the electrons have a loss-cone distribution at the maximum power of these two waves. Based on the electron distributions and linear theory, we infer that the whistler waves and the ECH waves are generated by the electron loss-cone instability.

Generally, the wave spectrum of ECH waves will not be exactly at the half-harmonics of the electron cyclotron frequency $(n + 1/2) f_{ce}$. It can be concentrated in the upper half of the harmonic frequency band between $(n + 1/2) f_{ce}$ and $(n + 1) f_{ce}$, or the lower half of the harmonic frequency band between $n f_{ce}$ and $(n + 1/2) f_{ce}$ (Zhou et al., 2017). In our observations, the wave spectrums of ECH waves are mainly centered in the upper band, and based on the linear theory, the frequencies corresponding to the maximum growth rate calculated by the linear theory are also in the upper band, but they are slightly smaller than the observations. In Zhou et al. (2017), we know that the electron temperature, background density, and wave normal angle all play an important role to produce the different wave spectrum, in which the frequency corresponding to the maximum growth rate will increase with the increase in the energetic electron temperature. Thus, we infer that the small deviations between the linear theory and the observation may be caused by the error of these parameters setting in the linear theory.

Data Availability Statement

The MMS data we used are available at the MMS data center (<https://lasp.colorado.edu/mms/sdc/>).

Acknowledgments

Our work is supported by the Strategic Priority Research Program of Chinese Academy of Sciences, Grant No. XDB 41000000, the NSFC grant 41774169.

References

- Ashour-Abdalla, M., & Kennel, C. F. (1978). Nonconvective and convective electron cyclotron harmonic instabilities. *Journal of Geophysical Research*, 83, 1531–1543. <https://doi.org/10.1029/JA083iA04p01531>
- Bell, T. F., & Buneman, O. (1964). Plasma instability in the whistler mode caused by a gyrating electron stream. *Physical Review*, 133, 1300–1302. <https://doi.org/10.1103/PhysRev.133.A1300>
- Breuillard, H., le Contel, O., Retino, A., Chasapis, A., Chust, T., Mirioni, L., et al. (2016). Multi spacecraft analysis of dipolarization fronts and associated whistler wave emissions using MMS data. *Geophysical Research Letters*, 43, 7279–7286. <https://doi.org/10.1002/2016GL069188>
- Burch, J. L., Torbert, R. B., Phan, T. D., Chen, L.-J., Moore, T. E., Ergun, R. E., et al. (2016). Electron-scale measurements of magnetic reconnection in space. *Science*, 352, aaf2939. <https://doi.org/10.1126/science.aaf2939>
- Cao, D., Fu, H. S., Cao, J. B., Wang, T. Y., Graham, D. B., Chen, Z. Z., et al. (2017). MMS observations of whistler waves in electron diffusion region. *Geophysical Research Letters*, 44, 3954–3962. <https://doi.org/10.1002/2017GL072703>
- Cattell, C., Dombeck, J., Wygant, J., Drake, J. F., Swisdak, M., Goldstein, M. L., et al. (2005). Cluster observations of electron holes in association with magnetotail reconnection and comparison to simulations. *Journal of Geophysical Research*, 110, A01211. <https://doi.org/10.1029/2004JA010519>
- Deng, X. H., & Matsumoto, H. (2001). Rapid magnetic reconnection in the Earth's magnetosphere mediated by whistler waves. *Nature*, 410(6828), 557–560. <https://doi.org/10.1038/35069018>
- Ergun, R. E., Tucker, S., Westfall, J., Goodrich, K. A., Malaspina, D. M., Summers, D., et al. (2016). The axial double probe and fields signal processing for the MMS mission. *Space Science Reviews*, 199(1–4), 167–188. <https://doi.org/10.1007/s11214-014-0115-x>
- Gao, X., Lu, Q., Bortnik, J., Li, W., Chen, L., & Wang, S. (2016). Generation of multiband chorus by lower band cascade in the Earth's magnetosphere. *Geophysical Research Letters*, 43, 2343–2350. <https://doi.org/10.1002/2016gl068313>
- Goldman, M. V., Newman, D. L., Lapenta, G., Andersson, L., Gosling, J. T., Eriksson, S., et al. (2014). Čerenkov emission of quasiparallel whistlers by fast electron phase-space holes during magnetic reconnection. *Physical Review Letters*, 112, 145002. <https://doi.org/10.1103/PhysRevLett.112.145002>
- Graham, D. B., Vaivads, A., Khotyaintsev, Y. V., & André, M. (2016). Whistler emission in the separatrix regions of asymmetric magnetic reconnection. *Journal of Geophysical Research: Space Physics*, 121, 1934–1954. <https://doi.org/10.1002/2015JA021239>
- Gurnett, D. A., Anderson, R. R., Tsurutani, B. T., Smith, E. J., Paschmann, G., Haerendel, G., et al. (1979). Plasma wave turbulence at the magnetopause: Observations from ISEE 1 and 2. *Journal of Geophysical Research*, 84, 7043–7058. <https://doi.org/10.1029/JA084iA12p07043>
- Gurnett, D. A., & Bhattacharjee, A. (2005). *Introduction to plasma physics: With space and laboratory applications*: Cambridge Univ. Press.
- Gurnett, D. A., Frank, L. A., & Lepping, R. P. (1976). Plasma waves in the distant magnetotail. *Journal of Geophysical Research*, 81, 6059–6071. <https://doi.org/10.1029/JA081i034p06059>
- Horne, R. B., Thorne, R. M., Meredith, N. P., & Anderson, R. R. (2003). Diffuse auroral electron scattering by electron cyclotron harmonic and whistler mode waves during an isolated substorm. *Journal of Geophysical Research*, 108(A7), 1290. <https://doi.org/10.1029/2002JA009736>
- Huang, S. Y., Fu, H. S., Yuan, Z. G., Vaivads, A., Khotyaintsev, Y. V., Retino, A., et al. (2016). Two types of whistler waves in the hall reconnection region. *Journal of Geophysical Research: Space Physics*, 121(7), 6639–6646. <https://doi.org/10.1002/2016ja022650>
- Huang, S. Y., Xu, S. B., He, L. H., Jiang, K., Yuan, Z. G., Deng, X. H., et al. (2020). Excitation of whistler waves through the bidirectional field-aligned electron beams with electron temperature anisotropy: MMS observations. *Geophysical Research Letters*, 47, e2020GL087515. <https://doi.org/10.1029/2020GL087515>
- Huang, S. Y., Yuan, Z. G., Sahraoui, F., Fu, H. S., Pang, Y., Zhou, M., et al. (2017). Occurrence rate of whistler waves in the magnetotail reconnection region. *Journal of Geophysical Research: Space Physics*, 122, 7188–7196. <https://doi.org/10.1002/2016JA023670>
- Jiang, K., Huang, S. Y., Yuan, Z. G., Yu, X. D., Liu, S., Deng, D., & He, L. H. (2019). Observations of whistler waves in two sequential flux ropes at the magnetopause. *Astrophysics and Space Science*, 364(10), 168. <https://doi.org/10.1007/s10509-019-3647-4>
- Kennel, C. F., & Petschek, H. E. (1966). Limit on stably trapped particle fluxes. *Journal of Geophysical Research*, 71, 1–28. <https://doi.org/10.1029/JZ071i001p00001>
- Kennel, C. F., Scarf, F. L., Fredricks, R. W., McGehee, J. H., & Coroniti, F. V. (1970). VLF electric field observations in the magnetosphere. *Journal of Geophysical Research*, 75(31), 6136–6152. <https://doi.org/10.1029/JA075i031p06136>
- Kurita, S., Miyoshi, Y., Cully, C. M., Angelopoulos, V., le Contel, O., Hikishima, M., & Misawa, H. (2014). Observational evidence of electron pitch angle scattering driven by ECH waves. *Geophysical Research Letters*, 41, 8076–8080. <https://doi.org/10.1002/2014GL061927>
- Lapenta, G., Berchem, J., Zhou, M., Walker, R. J., El-Alaoui, M., Goldstein, M. L., et al. (2017). On the origin of the crescent-shaped distributions observed by MMS at the magnetopause. *Journal of Geophysical Research: Space Physics*, 122, 2024–2039. <https://doi.org/10.1002/2016JA023290>
- Le Contel, O., Leroy, P., Roux, A., Coillot, C., Alison, D., Bouabdellah, A., et al. (2014). The search-coil magnetometer for MMS. *Space Science Reviews*, 199(1–4), 257–282. <https://doi.org/10.1007/s11214-014-0096-9>
- Le Contel, O., Retino, A., Breuillard, H., Mirioni, L., Robert, P., Chasapis, A., et al. (2016). Whistler mode waves and Hall fields detected by MMS during a dayside magnetopause crossing. *Geophysical Research Letters*, 43, 5943–5952. <https://doi.org/10.1002/2016GL068968>
- Li, W. Y., Graham, D. B., Khotyaintsev, Y. V., Vaivads, A., André, M., Min, K., et al. (2020). Electron Bernstein waves driven by electron crescents near the electron diffusion region. *Nature Communications*, 11(1), 141. <https://doi.org/10.1038/s41467-019-13920-w>
- Lindqvist, P.-A., Olsson, G., Torbert, R. B., King, B., Granoff, M., Rau, D., et al. (2014). The spin-plane double probe electric field instrument for MMS. *Space Science Reviews*, 199(1–4), 137–165. <https://doi.org/10.1007/s11214-014-0116-9>
- Liu, X., Chen, L., Gu, W., & Zhang, X.-J. (2018). Electron cyclotron harmonic wave instability by loss cone distribution. *Journal of Geophysical Research: Space Physics*, 123, 9035–9044. <https://doi.org/10.1029/2018JA025925>
- Lou, Y., Cao, X., Ni, B., Tu, W., Gu, X., Fu, S., et al. (2021). Diffuse auroral electron scattering by electrostatic electron cyclotron harmonic waves in the dayside magnetosphere. *Geophysical Research Letters*, 48, e2020GL092208. <https://doi.org/10.1029/2020GL092208>
- Lou, Y., Gu, X., Summers, D., Ni, B., Liu, K., Fu, S., et al. (2018). Statistical distributions of dayside ECH waves observed by MMS. *Geophysical Research Letters*, 45, 12730–12738. <https://doi.org/10.1029/2018GL0801210.1029/2018gl080125>
- Matsumoto, H., Deng, X. H., Kojima, H., & Anderson, R. R. (2003). Observation of Electrostatic Solitary Waves associated with reconnection on the dayside magnetopause boundary. *Geophysical Research Letters*, 30(6), 1326. <https://doi.org/10.1029/2002GL016319>
- Phan, T. D., Eastwood, J. P., Cassak, P. A., Øieroset, M., Gosling, J. T., Gershman, D. J., et al. (2016). MMS observations of electron-scale filamentary currents in the reconnection exhaust and near the X line. *Geophysical Research Letters*, 43, 6060–6069. <https://doi.org/10.1002/2016GL069212>

- Pollock, C., Moore, T., Jacques, A., Burch, J., Gliese, U., Saito, Y., et al. (2016). Fast plasma investigation for magnetospheric multiscale. *Space Science Reviews*, 199(1–4), 331–406. <https://doi.org/10.1007/s11214-016-0245-4>
- Russell, C. T., Anderson, B. J., Baumjohann, W., Bromund, K. R., Dearborn, D., Fischer, D., et al. (2016). The magnetospheric multiscale magnetometers. *Space Science Reviews*, 199(1–4), 189–256. <https://doi.org/10.1007/s11214-014-0057-3>
- Sang, L. L., Lu, Q. M., Wang, R. S., Huang, K., & Wang, S. (2019). A Parametric study of the structure of hall magnetic field based on kinetic simulations. I. Anti-parallel magnetic reconnection in an asymmetric current sheet. *The Astrophysical Journal*, 877(2), 155. <https://doi.org/10.3847/1538-4357/ab14ef>
- Sonnerup, B. U. Ö., & Scheible, M. (1998). Minimum and maximum variance analysis. In G. Paschmann, & P. W. Daly (Eds.), *Analysis methods for multi spacecraft data* (pp. 185–215). European Space Agency.
- Stenzel, R. L. (1999). Whistler waves in laboratory plasmas. *Journal of Geophysical Research*, 104(A7), 14379–14396. <https://doi.org/10.1029/1998ja900120>
- Tang, X., Cattell, C., Dombeck, J., Dai, L., Wilson, L. B., III, Breneman, A., & Hupach, A. (2013). THEMIS observations of the magnetopause electron diffusion region: Large amplitude waves and heated electrons. *Geophysical Research Letters*, 40, 2884–2890. <https://doi.org/10.1002/grl.50565>
- Thorne, R. M., Ni, B., Tao, X., Horne, R. B., & Meredith, N. P. (2010). Scattering by chorus waves as the dominant cause of diffuse auroral precipitation. *Nature*, 467, 943–946. <https://doi.org/10.1038/nature09467>
- Umeda, T., Ashour-Abdalla, M., Schriver, D., Richard, R. L., & Coroniti, F. V. (2007). Particle-in-cell simulation of Maxwellian ring velocity distribution. *Journal of Geophysical Research: Space Physics*, 112, A04212. <https://doi.org/10.1029/2006JA012124>
- Vaivads, A., Santolik, O., Stenberg, G., André, M., Owen, C. J., Canu, P., & Dunlop, M. (2007). Source of whistler emissions at the dayside magnetopause. *Geophysical Research Letters*, 34, L09106. <https://doi.org/10.1029/2006GL029195>
- Viberg, H., Khotyaintsev, Y. V., Vaivads, A., André, M., & Pickett, J. S. (2013). Mapping HF waves in the reconnection diffusion region. *Geophysical Research Letters*, 40, 1032–1037. <https://doi.org/10.1002/grl.50227>
- Wang, R., Lu, Q., Khotyaintsev, Y. V., Volwerk, M., Du, A., Nakamura, R., et al. (2014). Observation of double layer in the separatrix region during magnetic reconnection. *Geophysical Research Letters*, 41, 4851–4858. <https://doi.org/10.1002/2014GL061157>
- Wang, R., Nakamura, R., Lu, Q., Baumjohann, W., Ergun, R. E., Burch, J. L., et al. (2017). Electron-scale quadrants of the hall magnetic field observed by the magnetospheric multiscale spacecraft during asymmetric reconnection. *Physical Review Letters*, 118, 175101. <https://doi.org/10.1103/PhysRevLett.118.175101>
- Wang, S., Wang, R., Yao, S. T., Lu, Q., Russell, C. T., & Wang, S. (2019). Anisotropic electron distributions and whistler waves in a series of the flux transfer events at the magnetopause. *Journal of Geophysical Research: Space Physics*, 124, 1753–1769. <https://doi.org/10.1029/2018JA026417>
- Wilder, F. D., Ergun, R. E., Goodrich, K. A., Goldman, M. V., Newman, D. L., Malaspina, D. M., et al. (2016). Observations of whistler mode waves with nonlinear parallel electric fields near the dayside magnetic reconnection separatrix by the Magnetospheric Multiscale mission. *Geophysical Research Letters*, 43, 5909–5917. <https://doi.org/10.1002/2016GL069473>
- Wu, Y., Tao, X., Liu, X., Chen, L., Xie, H., Liu, K., & Horne, R. B. (2020). Particle-in-cell simulation of electron cyclotron harmonic waves driven by a loss cone distribution. *Geophysical Research Letters*, 47, e2020GL087649. <https://doi.org/10.1029/2020GL087649>
- Xie, H. S. (2019). BO: A unified tool for plasma waves and instabilities analysis. *Computer Physics Communications*, 244, 343–371. <https://doi.org/10.1016/j.cpc.2019.06.014>
- Yu, X., Lu, Q., Wang, R., Huang, K., Gao, X., & Wang, S. (2021). MMS observations of broadband electrostatic waves in electron diffusion region of magnetotail reconnection. *Journal of Geophysical Research: Space Physics*, 126, e2020JA028882. <https://doi.org/10.1029/2020JA028882>
- Yu, X., Wang, R., Lu, Q., Russell, C. T., & Wang, S. (2019). Nonideal electric field observed in the separatrix region of a magnetotail reconnection event. *Geophysical Research Letters*, 46, 10744–10753. <https://doi.org/10.1029/2019GL082538>
- Zhao, S. Q., Xiao, C. J., Liu, T. Z., Chen, H., Zhang, H., Shi, M. J., et al. (2021). Observations of the beam-driven whistler mode waves in the magnetic reconnection region at the dayside magnetopause. *Journal of Geophysical Research: Space Physics*, 126, e2020JA028525. <https://doi.org/10.1029/2020JA028525>
- Zhong, Z. H., Graham, D. B., Khotyaintsev, Y. V., Zhou, M., Le Contel, O., Tang, R. X., & Deng, X. H. (2021). Whistler and broadband electrostatic waves in the multiple X-line reconnection at the magnetopause. *Geophysical Research Letters*, 48, e2020GL091320. <https://doi.org/10.1029/2020GL091320>
- Zhou, M., Ashour-Abdalla, M., Berchem, J., Walker, R. J., Liang, H., El-Alaoui, M., et al. (2016). Observation of high-frequency electrostatic waves in the vicinity of the reconnection ion diffusion region by the spacecraft of the Magnetospheric Multiscale (MMS) mission. *Geophysical Research Letters*, 43, 4808–4815. <https://doi.org/10.1002/2016GL069010>
- Zhou, M., Ashour-Abdalla, M., Deng, X., Schriver, D., El-Alaoui, M., & Pang, Y. (2009). THEMIS observation of multiple dipolarization fronts and associated wave characteristics in the near-Earth magnetotail. *Geophysical Research Letters*, 36, L20107. <https://doi.org/10.1029/2009GL040663>
- Zhou, M., Pang, Y., Deng, X. H., Yuan, Z. G., & Huang, S. Y. (2011). Density cavity in magnetic reconnection diffusion region in the presence of guide field. *Journal of Geophysical Research*, 116, A06222. <https://doi.org/10.1029/2010JA016324>
- Zhou, Q., Xiao, F., Yang, C., Liu, S., He, Y., Baker, D. N., et al. (2017). Generation of lower and upper bands of electrostatic electron cyclotron harmonic waves in the Van Allen radiation belts. *Geophysical Research Letters*, 44, 5251–5258. <https://doi.org/10.1002/2017GL073051>